

Integrated metamaterials for efficient and compact free-space-to-waveguide coupling

Bing Shen,¹ Peng Wang,¹ Randy Polson,² and Rajesh Menon^{1,*}

¹Department of Electrical and Computer Engineering, University of Utah, Salt Lake City, UT 84112, USA

²Utah Nanofabrication Facility, University of Utah, Salt Lake City, UT 84112, USA

rmenon@eng.utah.edu

Abstract: We applied nonlinear optimization to design nanophotonics-based metamaterials for efficient free-space-to-waveguide coupling. Three devices were designed, fabricated and characterized. The first device couples incident light into a multi-mode waveguide, the second device couples incident light into a single-mode waveguide directly, and the third device couples and separates two orthogonal polarizations into two multi-mode waveguides. All devices offer comparable or higher coupling efficiencies, are easier to fabricate, and demonstrate higher bandwidth when compared to conventional devices. Furthermore, each device is at least an order of magnitude smaller in area than previously reported devices. The highly efficient single-mode waveguide-coupler is a unique device that has not been experimentally demonstrated before. We further performed careful simulations to underscore the tolerance of these devices to fabrication errors. Their robustness is primarily a result of the large number of coupled guided-mode resonances that are responsible for each device performance.

©2014 Optical Society of America

OCIS codes: (350.4238) Nanophotonics and photonic crystals; (050.1970) Diffractive optics; (350.3950) Micro-optics.

References and links

1. T. Shoji, T. Tsuchizawa, T. Watanabe, K. Yamada, and H. Morita, "Low loss mode size converter from 0.3 μm square Si wire waveguides to singlemode fibers," *Electron. Lett.* **38**(25), 1669–1670 (2002).
2. S. McNab, N. Moll, and Y. Vlasov, "Ultra-low loss photonic integrated circuit with membrane-type photonic crystal waveguides," *Opt. Express* **11**(22), 2927–2939 (2003).
3. N. Fang, Z. Yang, A. Wu, J. Chen, M. Zhang, S. Zou, and X. Wang, "Three-dimensional tapered spot-size converter based on (111) silicon-on-insulator," *IEEE Photon. Technol. Lett.* **21**(12), 820–822 (2009).
4. M. Pu, L. Liu, H. Ou, K. Yvind, and J. M. Hvam, "Ultra-low-loss inverted taper coupler for silicon-on-insulator ridge waveguide," *Opt. Commun.* **283**(19), 3678–3682 (2010).
5. R. Takei, M. Suzuki, E. Omoda, S. Manako, T. Kamei, M. Mori, and Y. Sakakibara, "Silicon knife-edge taper waveguide for ultralow-loss spot-size converter fabricated by photolithography," *Appl. Phys. Lett.* **102**(10), 101108 (2013).
6. D. Taillaert, W. Bogaerts, P. Bienstman, T. F. Krauss, P. Van Daele, I. Moerman, S. Versteuyft, K. De Mesel, and R. Baets, "An out-of-plane grating coupler for efficient butt-coupling between compact planar waveguides and single-mode fibers," *IEEE J. Quantum Electron.* **38**(7), 949–955 (2002).
7. D. Taillaert, W. Bogaerts, and R. Baets, "Efficient coupling between submicron SOI-waveguides and singlemode fibers," in *Proceedings of Symposium IEEE/LEOS Benelux Chapter*, Enschede, The Netherlands (2003), pp. 289–292.
8. W. Bogaerts, D. Taillaert, B. Luyssaert, P. Dumon, J. Van Campenhout, P. Bienstman, D. Van Thourhout, R. Baets, V. Wiaux, and S. Beckx, "Basic structures for photonic integrated circuits in Silicon-on-insulator," *Opt. Express* **12**(8), 1583–1591 (2004).
9. G. Z. Masanovic, G. T. Reed, W. Headley, B. Timotijevic, V. M. Passaro, R. Atta, G. Ensell, and A. G. Evans, "A high efficiency input/output coupler for small silicon photonic devices," *Opt. Express* **13**(19), 7374–7379 (2005).
10. F. Van Laere, G. Roelkens, M. Ayre, J. Schrauwen, D. Taillaert, D. Van Thourhout, T. F. Krauss, and R. Baets, "Compact and highly efficient grating couplers between optical fiber and nanophotonic waveguides," *J. Lightwave Technol.* **25**(1), 151–156 (2007).

11. S. K. Selvaraja, D. Vermeulen, M. Schaekers, E. Sleetx, W. Bogaerts, G. Roelkens, P. Dumon, D. Van Thourhout, and R. Baets, "Highly efficient grating coupler between optical fiber and silicon photonic circuit," in *Conference on Lasers and Electro-Optics*, Baltimore, Maryland (2009), CTuC6.
12. X. Chen, C. Li, C. K. Fung, S. M. Lo, and H. K. Tsang, "Apodized waveguide grating couplers for efficient coupling to optical fibers," *IEEE Photon. Technol. Lett.* **22**(15), 1156–1158 (2010).
13. A. Mekis, S. Gloeckner, G. Masini, A. Narasimha, T. Pinguet, S. Sahni, and P. De Dobbelaere, "A grating coupler-enabled CMOS photonics platform," *IEEE J. Sel. Top. Quantum Electron.* **17**(3), 597–608 (2011).
14. A. Mekis, S. Abdalla, D. Foltz, S. Gloeckner, S. Hovey, S. Jackson, Y. Liang, M. Mack, G. Masini, M. Peterson, T. Pinguet, S. Sahni, M. Sharp, P. Sun, D. Tan, L. Verslegers, B. P. Welch, K. Yokoyama, S. Yu, and P. M. De Dobbelaere, "A CMOS photonics platform for high-speed optical interconnects," in *Proceedings of IEEE Photonics Conference* (2012), pp. 356–357.
15. C. Zhang, J.-H. Sun, X. Xiao, W.-M. Sun, X.-J. Zhang, T. Chu, J.-Z. Yu, and Y.-D. Yu, "High efficiency grating coupler for coupling between single-mode fiber and SOI waveguides," *Chin. Phys. Lett.* **30**(1), 014207 (2013).
16. W. S. Zaoui, A. Kunze, W. Vogel, M. Berroth, J. Butschke, F. Letzkus, and J. Burghartz, "Bridging the gap between optical fibers and silicon photonic integrated circuits," *Opt. Express* **22**(2), 1277–1286 (2014).
17. J. Lu and J. Vučković, "Nanophotonic computational design," *Opt. Express* **21**(11), 13351–13367 (2013).
18. F. Van Laere, T. Claes, J. Schrauwen, S. Scheerlinck, W. Bogaerts, D. Taillaert, L. O'Faolain, D. Van Thourhout, and R. Baets, "Compact focusing grating couplers for silicon-on-insulator integrated circuits," *IEEE Photon. Technol. Lett.* **19**(23), 1919–1921 (2007).
19. G. Kim, J.-A. Dominguez-Caballero, H. Lee, D. J. Friedman, and R. Menon, "Increased photovoltaic power output via diffractive spectrum separation," *Phys. Rev. Lett.* **110**(12), 123901 (2013).
20. P. Wang and R. Menon, "Optimization of generalized dielectric nanostructures for enhanced light trapping in thin-film photovoltaics via boosting the local density of optical states," *Opt. Express* **22**(S1), A99–A110 (2014).
21. B. Shen, P. Wang, and R. Menon, "Optimization and analysis of 3D nanostructures for power-density enhancement in ultra-thin photovoltaics under oblique illumination," *Opt. Express* **22**(S2), A311–A319 (2014).
22. X. Wang, W. Shi, S. Grist, H. Yun, N. A. F. Jaeger, and L. Chrostowski, "Narrow-Band Transmission Filter using Phase-Shifted Bragg Gratings in SOI Waveguide," in *Proceedings of IEEE Photonics Conference* (2011), pp. 869–870.
23. Y. Li, D. Vermeulen, Y. De Koninck, G. Yurtsever, G. Roelkens, and R. Baets, "Compact grating couplers on silicon-on-insulator with reduced backreflection," *Opt. Lett.* **37**(21), 4356–4358 (2012).
24. Refractive index for silicon and silica, <http://refractiveindex.info/>.

1. Introduction

Silicon on insulator (SOI) is a promising material for high-density photonic-integrated circuits because of the large refractive-index contrast. However, coupling light from free space onto a photonic chip is highly inefficient. This is primarily due to the large area-mismatch between the free-space mode from an optical fiber ($\sim 78\mu\text{m}^2$) and that in an SOI waveguide ($\sim 0.125\mu\text{m}^2$). Furthermore, in order to match the momentum of the wave vectors, subwavelength diffractive structures are required. Several methods have been proposed to solve this problem [1–16]. Among them, the subwavelength grating coupler has arguably been the most successful [6]. Various types of grating couplers, including dual grating-assisted directional coupling [9], metal mirrors [10,16], distributed-Bragg reflectors (DBRs) [11], and apodized gratings [12–15], have been proposed to increase the coupling efficiency. The highest coupling efficiency of a grating coupler reported is -0.62dB and the size of this device is $15\mu\text{m} \times 15.2\mu\text{m}$ [16]. However, this device required a separate backside metal mirror, which complicates the fabrication process. Furthermore, the standard grating couplers require a separate aligned lithography and etching step, since the depth of the grating is typically smaller than that of the waveguides themselves. Related forms of mode converters with coupling efficiency of -0.5dB have also been proposed [1,3]. However, these devices are very large (a few hundred micrometers in length), which greatly limit their applicability in integrated photonics.

Free-form metamaterials offer a new degree of design freedom, which can enable unique and efficient integrated-photonic applications in a very compact area [17]. The basic premise of this approach is that via nanofabrication, one can control the local refractive index of the device. By spatial engineering of the refractive index, it is possible to design devices such as the free-space-to-waveguide coupler with much higher performance that is otherwise possible. In this paper, we design, fabricate and characterize three metamaterial couplers. In each device, the input is normally incident from out of plane. The output is coupled into one or

more waveguides. All devices are designed for $\lambda_0 = 1550\text{nm}$ and are fabricated on a SOI substrate with a silicon thickness of 300nm and an oxide thickness of $3\mu\text{m}$. The first device is illustrated in Fig. 1(a). This device is comprised of 30×30 square pixels, each of size $100\text{nm} \times 100\text{nm}$, resulting in a total device area of $3\mu\text{m} \times 3\mu\text{m}$. Linearly polarized (electric field along Y) incident light is coupled into the multi-mode waveguide (width = $3\mu\text{m}$) with a simulated efficiency of -0.65dB , only slightly lower than the best reported efficiency to date for such a device. The simulated time-averaged intensity distribution is shown in Fig. 1(b). The field distributions seem to indicate that the mode coupling is primarily enabled by the excited guided-mode resonances in the structures. The refractive index variation introduced by the metamaterial coupler creates a perturbation of the incoming wave front. As a result, multiple guided-mode resonances are excited so as to match the wave vectors of the waveguide-propagation modes. In Fig. 1(a), the white regions represent air, where the silicon has been etched away (black regions represents unetched silicon) and the etch depth is the same as the depth of the waveguide, 300nm . In other words, the device can be fabricated at the same time as the waveguides, and a separate lithography and etch step is no longer required. Note that in the previous best device, the grating is shallower than the waveguide, necessitating a separate aligned lithography and etch step [16]. Furthermore, the previous best device also requires a backside metal mirror, which is not required in our device.

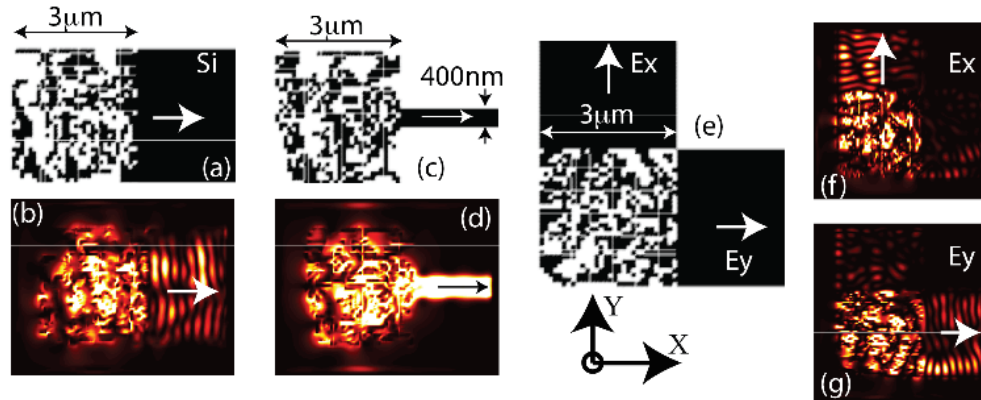


Fig. 1. Metamaterial coupler designs. (a) Free-space to multi-mode waveguide coupler and (b) corresponding simulated time-averaged intensity distribution (see Media 1). (c) Free-space to single-mode waveguide coupler and (d) corresponding simulated time-averaged intensity distribution (see Media 2). (e) Free-space to multi-mode waveguide coupler and polarization splitter. Simulated time-averaged intensity distribution for light polarized along X and that polarized along Y are shown in (f) (see Media 3) and (g) (see Media 4), respectively. For (b) and (d), light is linearly polarized along Y-axis, while for (f) and (g), light is randomly polarized. In all cases, $\lambda_0 = 1550\text{nm}$ and light is normally incident from out of the plane of the figure. The arrows represent direction of light propagation in the waveguides.

The second device is illustrated in Fig. 1(c). Normally incident linearly polarized (electric field along Y) light is coupled directly into a single-mode waveguide (width = 400nm) as illustrated by the simulated time-averaged intensity distribution in Fig. 1(d). This device exhibits a simulated coupling efficiency of -3dB , which is far higher than the efficiency reported previously [18]. The device reported in ref [18] requires a gold grating and is substantially larger than our device. A theoretical design was also previously described with a coupling efficiency of about -3dB [17]. However, this design is extremely challenging to fabricate due to the required continuous contours. In conventional integrated photonics, a very long adiabatic taper (millimeters in length) is required to do mode conversion from a multi-mode to a single-mode waveguide [8]. The third device shown in Fig. 1(e) is a combined coupler and polarization splitter. The incident light is again normally incident but is comprised of two orthogonal polarizations. The device couples one polarization into one

multi-mode waveguide and the other polarization into the second multi-mode waveguide, as illustrated by the simulated time-averaged intensity distributions in Figs. 1(f) and 1(g) for E_x and E_y polarizations, respectively. The simulated coupling efficiency averaged over both polarizations for this device is -1.5dB , which is higher than that for a comparable device reported previously ($\sim -3.2\text{dB}$) [13].

2. Design

We applied a modified version of the direct-binary-search (DBS) algorithm to design the metamaterial couplers. DBS is an iterative search algorithm that we have previously utilized for designing broadband non-imaging optics [19] as well as nanophotonic light-trapping structures [20,21]. In order to apply this method, we have to discretize the device into “pixels.” As mentioned earlier, each metamaterial coupler is comprised of 30×30 square pixels, where each pixel is $100\text{nm} \times 100\text{nm}$. The pixel may be comprised entirely of silicon or of air (when the silicon is completely etched away). During each step of the DBS algorithm, the pixel is toggled between these two states and the figure-of-merit (FOM) for the device is evaluated. The pixel to be perturbed is chosen at random. The FOM is defined as the coupling efficiency. If the FOM is improved, the pixel state is retained. Otherwise, the pixel state is toggled and the search continues. Each iteration of the DBS algorithm is comprised of the perturbation of all 900 pixels. The iterations stop when no device improvement is achieved or if the improvement is smaller than a previously specified threshold. Note that fabrication constraints are naturally incorporated into the algorithm due to the discrete nature of the pixels. The choice of pixel size is driven by the capability of the fabrication tool. We parallelized the search algorithm and utilized Amazon’s EC2 cloud service to expedite the simulations. Three virtual machines each with 32 virtual CPUs were used to construct a micro cluster for parallel computation and one optimization took about 300 hours. In general, increasing the number of degrees of freedom, either by decreasing the pixel size and/or increasing the device area significantly improves the performance of the device. However, this comes at the expense of computation time and the DBS algorithm could get trapped in local maxima when the search-space is increased. Multiple random initial guesses may be used to minimize the impact of the latter effect. In any case, the DBS algorithm has the advantage that it is guaranteed to converge to a solution. We picked a device size of $3\mu\text{m} \times 3\mu\text{m}$ to illustrate the efficacy of our design approach. An open-source finite-difference time-domain (FDTD) solver (MEEP) was used to simulate the full 3D geometry of our designs. Note that we utilize a normally incident plane wave as the input for each device. However, our approach can be readily extended to include focused light input as well.

3. Experiments

Our devices are fabricated on a silicon-on-insulator (SOI) wafer with a silicon thickness of 300nm . Although the devices could be patterned using a single lithography and etch step, since we do not have access to a tool that has the requisite resolution over millimeter-sized areas, we opted for a two-step fabrication process. We first used the Heidelberg MicroPG 101 (laser pattern generator) to pattern the $3\mu\text{m}$ -wide waveguide patterns in positive photoresist (Shipley 1813) deposited on top of the silicon layer. The exposure power was 10mW at 65% duration factor and bi-directional mode was employed. Standard 352B developer was used to develop the photoresist for 1min. Then, an Oxford 100 reactive-ion etcher (RIE) was used to etch the silicon. The gas was a mixture of SF_6 with a flow rate of 40ccm and CF_4 with a flow rate of 17.5ccm . SF_6 is used for etching the silicon, while CF_4 is used for passivation during etching in order to get straight sidewalls. For our sample, the total etch time was 240 seconds that corresponds to an etch rate of 1.25nm per second. Then, we used the dual-beam focused-ion-beam (FEI, Helios 650) system to define the metamaterial couplers, the single-mode waveguide and any associated tapers. The metamaterial couplers have a minimum feature size of 100nm . The ion beam accelerating voltage was 30kV for all devices. For the metamaterial

couplers, the beam current used was 7.7pA with fluence of 800C/m². Alignment marks were used to ensure that the metamaterial couplers were appropriately aligned with the waveguides. We also fabricated reference devices with conventional grating couplers for comparison with the metamaterial couplers [22]. The reference grating coupler was etched to a shallower depth (80nm) using the FIB and the corresponding beam current was 24pA with a fluence of 220C/m².

Since all output light measurements were performed using butt-coupling, we also designed and fabricated a 4μm-long taper from the single-mode waveguide (for the device in Fig. 1(c)) to a 3μm-wide multi-mode waveguide. Scanning-electron micrographs of the 3 devices are shown in Figs. 2(a)–2(c). The measured sizes of the pixels in the metamaterials devices range from 95nm to 110nm.

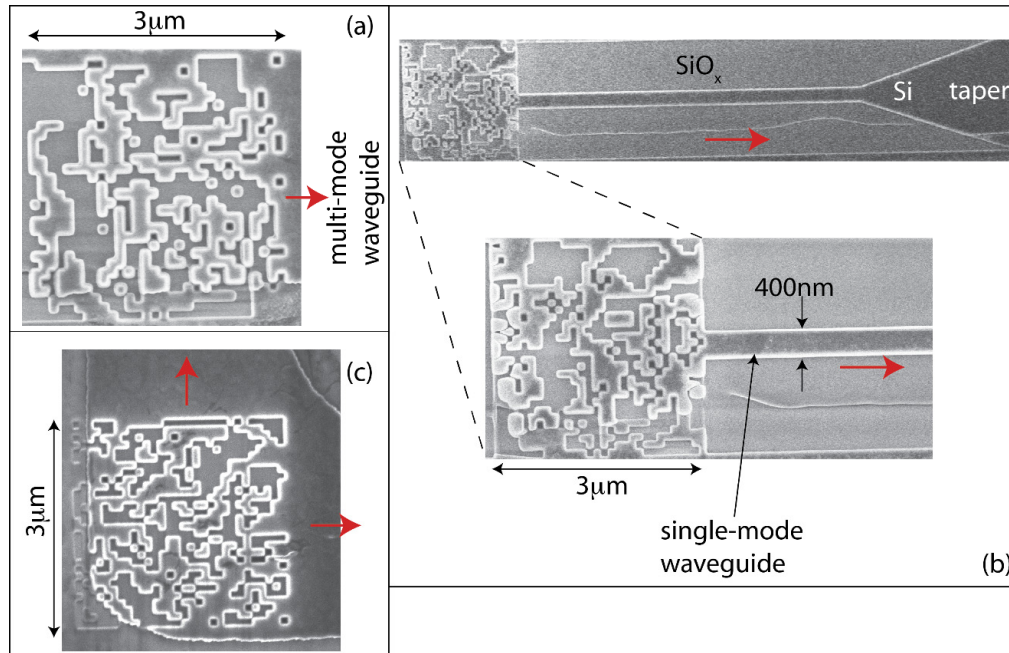


Fig. 2. Scanning-electron micrographs of fabricated devices. (a) Free-space to multi-mode waveguide coupler. (b) Free-space to single-mode waveguide coupler. Note the taper from single-mode to multi-mode waveguide to facilitate butt coupling in order to measure the output. (c) Free-space to multi-mode waveguide coupler and polarization splitter. Red arrows indicate the direction of coupled (output) light flow.

For measurement, we used a fiber-coupled laser (Hewlett Packard Model No. 8168E) with center wavelength of 1550nm. The light output from a fiber collimator was normally incident on each metamaterial coupler. The mode-field diameter of the collimated beam is 0.9mm. The output light was measured by butt-coupling from a multi-mode waveguide (width = 3μm) using a lensed fiber. A polarizer was used at the input to check the response of the device for each polarization separately. The reference device was comprised of a waveguide of width = 3μm and the same overall length as the waveguides used with the metamaterial couplers. The reference grating coupler had a period of 700nm, duty cycle of 50% and an etch depth of 80nm [22]. The reference coupler was fabricated using FIB but a lower dose was used compared to the metamaterial couplers. An incident angle of ~8° was used for the reference grating coupler as this configuration achieved the highest coupling efficiency [23]. We measured the output power from the metamaterial couplers relative to the reference grating coupler. Then, we used the simulated coupling efficiency spectrum of the reference device to estimate the absolute coupling efficiencies of the metamaterial devices. Furthermore, for the

single-mode coupler, we accounted for the taper loss via simulations. The resulting experimental and simulated coupling efficiencies as a function of the incident wavelength are plotted in Figs. 3(a)–3(c) for the 3 devices in Figs. 2(a)–2(c), respectively.

The measured efficiencies are slightly lower than the expected values, but otherwise agree well overall. The discrepancies are likely due to the fabrication errors and edge roughness in the devices. These can be mitigated in the future by optimizing the patterning and etching processes. The ripples in the measured efficiencies are likely due to the Fabry-Perot resonance between light reflection from the fiber and that from the fabricated devices. Nevertheless, we measured peak-coupling efficiencies of -1.25dB and -3.9dB for the multi-mode and single-mode couplers, respectively. The measured peak-coupling efficiencies for the coupler/polarization splitter device are -1.97dB for E_x and -2.63dB for E_y , respectively. The extinction-ratio spectra for the free-space to multi-mode coupler and polarization splitter are shown in Fig. 4. The measured extinction ratios for the two outputs (E_x and E_y) at the design wavelengths are 6.4dB and 4.3dB , respectively.

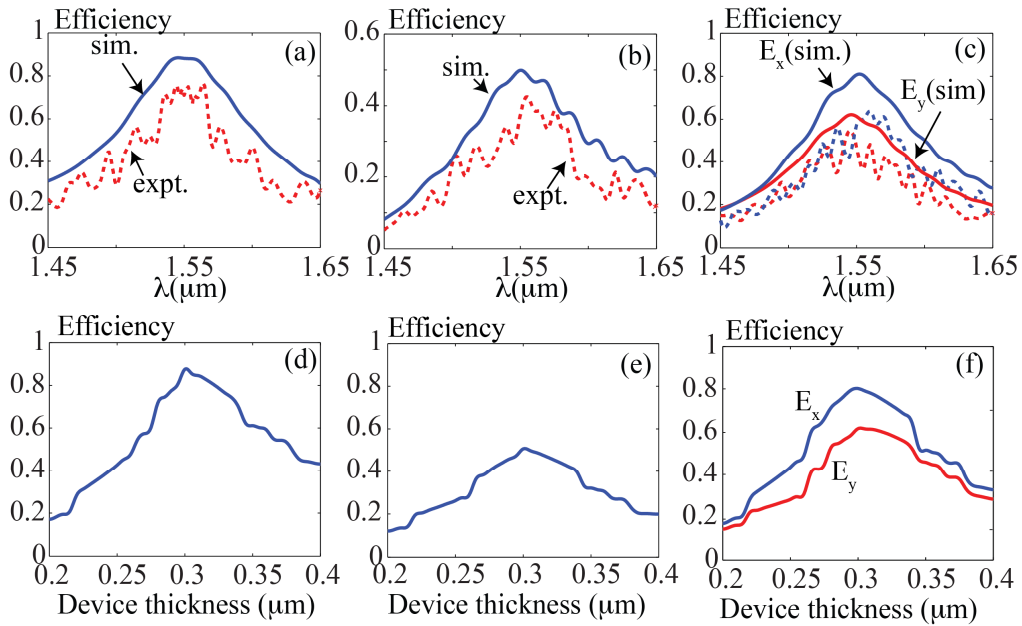


Fig. 3. Measured (expt.) and simulated (sim.) efficiencies of (a) free-space to multi-mode coupler, (b) free-space to single-mode coupler and (c) free-space to multi-mode coupler and polarization splitter. In (c), the X and Y polarizations are shown in blue and red, respectively. In all plots, the simulation and experimental data are shown using solid and dashed lines, respectively. Simulated efficiencies as a function of the device thickness for (d) free-space to multi-mode coupler, (e) free-space to single-mode coupler and (f) free-space to multi-mode coupler and polarization splitter.

4. Discussion

From the simulated efficiency plot in Fig. 3(a), we can estimate the 1dB bandwidth of the device as 64nm (1519nm to 1583nm). The 1dB bandwidth for the free-space to single-mode coupler is 49nm (1527nm to 1576nm). In the case of the polarization-separating coupler, the 1dB bandwidth is 56nm (1524nm to 1574nm) for E_x and 55nm (1519nm to 1574nm) for E_y . In comparison, the previous best grating coupler exhibits a 1dB bandwidth of $\sim 40\text{nm}$ [16]. Our devices exhibit a larger bandwidth due to the fact the mechanism of multiple coupled guided modes is responsible for the coupling. The multiple resonances enable the device to be less sensitive to wavelength shifts. In contrast, with single resonant-mode devices (like the conventional grating couplers), a small shift in wavelength will result in mode-mismatch and

severely lower coupling efficiency. Therefore, adjusting the tilt angle of the fiber is needed to correct any wavelength shift. The dispersion data for silicon used in the simulations is taken from ref [24].

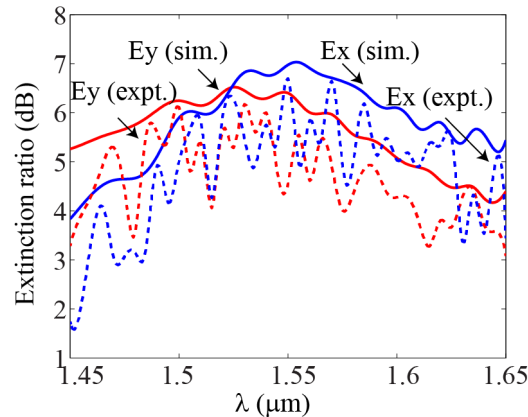


Fig. 4. Simulated (solid line) and measured (dashed line) extinction ratio of free-space to multi-mode coupler and polarization splitter.

We also numerically investigated the robustness of our designs to fabrication errors. Specifically, we varied the thickness of the device (determined by the etch depth of the pixels). The resulting coupling efficiency plots are shown in Figs. 3(d)–3(f) for the 3 devices, respectively. As expected, the efficiencies drop as the device thickness changes from the design value of 300nm. If we are able to tolerate an efficiency drop of 20% from the peak value, we can determine the appropriate specification for variation in device thickness. This allowable thickness variation is 59nm (–20nm to + 39nm) for the free-space to multi-mode coupler, 63nm (–25nm to + 38nm) for the free-space to single-mode coupler and 67nm (–27nm to + 40nm) for the coupler/polarization-splitter. In addition, we used simulations to study the impact of the alignment error between the waveguides and the couplers. We conclude that a 100nm alignment error results in ~0.3dB drop of the coupling efficiency for each polarization state.

We also simulated the time evolution of the electric fields within this device in order to visualize the performance of the device. The resulting animations for all 3 devices are included as supplementary videos. The input plane wave is normally incident on each device as discussed earlier. Due to the subwavelength structures within each device, evanescent modes are excited. These evanescent modes act in a concerted fashion and give rise to multiple resonant modes that are propagating in the plane of the device. The multiple resonant modes result in mode excitation in the output waveguide. The geometry of each metamaterial coupler is optimized to enhance the overall power transfer from the incident light into the appropriate output waveguide.

5. Conclusion

We designed metamaterial couplers that efficiently redirect light from free-space into integrated waveguides using a novel extension of the direct-binary-search algorithm. The algorithm is able to incorporate fabrication constraints, which results in practical and error-tolerant devices. The devices themselves are compatible with conventional optical lithography used to manufacture CMOS devices, and the coupler thickness is the same as the waveguide thickness. Due to the limitations of the tools available to us, we used a combination of optical lithography and focused-ion-beam lithography to fabricate our devices. We characterized the devices and experimentally demonstrated coupling efficiencies of –1.25dB for a free-space to multi-mode waveguide coupler, –3.9dB for a free-space to single-mode waveguide coupler

and -1.97dB and -2.63dB for a free-space to multi-mode waveguide coupler and polarization splitter for E_x and E_y polarizations, respectively. The efficiency of each device is at least comparable to, if not larger than that of previously reported devices. This is achieved even though our devices are considerably smaller than the previous ones. In addition, our devices demonstrate higher bandwidths and better robustness to fabrication errors. Our design technique is readily extended to many other standard and unique passive integrated-photonics devices and can be applied to not only enhance efficiency but also increase the device-integration density and functionality.